



Driving hydrogen peroxide artificial photosynthesis and utilization for emerging contaminants removal by cyanided polymeric carbon nitride

Yunfei Ma^{a,1}, Hongli Sun^{a,1}, Qizhen Wang^b, Like Sun^a, Zailun Liu^a, Yao Xie^a, Qitao Zhang^{a,*}, Chenliang Su^a, Dianyuan Fan^a

^a International Collaborative Laboratory of 2D Materials for Optoelectronics Science and Technology of Ministry of Education, Key Laboratory of Optoelectronic Devices and Systems of Ministry of Education and Guangdong Province, Institute of Microscale Optoelectronics, Shenzhen University, Shenzhen 518060, China

^b Nanophotonics Research Center, Shenzhen Key Laboratory of Micro-Scale Optical Information Technology & Institute of Microscale Optoelectronics, Shenzhen University, Shenzhen 518060, China

ARTICLE INFO

Keywords:

Cyano group
Polymeric Carbon Nitride
O₂ Reduction
H₂O₂ Photosynthesis
ECs

ABSTRACT

To unravel the influence of the structure-activity relationship (SAR) of cyano (-C≡N) groups on the photocatalytic activity of polymeric carbon nitride (PCN), -C≡N groups were controllably introduced and finely regulated within the PCN framework in this study. The SAR between the -C≡N contents and hydrogen peroxide (H₂O₂) artificial photosynthesis performance was conclusively confirmed. Comprehensive experimental characterization and theoretical calculations demonstrated that the introduced -C≡N accelerated the dissociation of excitons to free charge carriers. The excitons dissociation efficiency was enhanced twofold, and the adsorption and activation of O₂ molecules were strengthened, driving the two-electron O₂ reduction reaction (2e⁻ ORR) to produce H₂O₂. Importantly, the on-site generation of abundant reactive oxygen species during 2e⁻ ORR by the cyanided PCN photocatalyst demonstrated its outstanding performance for the removal of multifarious emerging contaminants (ECs), including 4-hydroxybenzoic acid, aspirin, and ibuprofen, to realize sustainable water purification.

1. Introduction

As an important green and high-value multifunctional oxidant, hydrogen peroxide (H₂O₂) is widely applied in a diverse range of industries, such as chemical synthesis, medical disinfection, wastewater treatment, and energy-related applications [1–4]. However, H₂O₂ is currently mainly manufactured by the anthraquinone method, which utilizes complex and large-scale infrastructure and produces a substantial volume of waste chemicals [5–7]. In comparison, the photocatalytic synthesis of H₂O₂ using semiconductor materials has emerged as a green, safe, environmentally friendly, and sustainable alternative method. Recently, polymeric carbon nitride (PCN) has been acknowledged as a state-of-the-art polymeric semiconductor material for the artificial photosynthesis of H₂O₂ from H₂O and O₂ due to its high stability, metal-free composition, facile synthesis, and unique optical/electronic structures [1,2,7,8]. Regrettably, PCN typically suffers from severe photogenerated carrier recombination and inferior selectivity for the two-electron oxygen reduction reaction (2e⁻ ORR), meaning that

enhancing the photoactivity of PCN remains a significant challenge.

Consequently, tuning the structure of PCN is highly desirable to promote its activity and assess its structure-activity relationship (SAR) [9–12]. Among the various structure tuning approaches, defect engineering has been demonstrated to be an efficient strategy for boosting the performance of PCN in applications such as photocatalytic H₂ evolution [13], CO₂ reduction [14,15], organic synthesis [16,17] and the removal of volatile organic compounds (VOCs) [7,18–24]. Modifying of PCN by introducing surface defects, such as surface vacancies (C [25,26] or N [2,27,28] vacancies) and surface functional groups (-C≡N [29–32], -COOH [32] or -NH₂ [33,34]), can positively or negatively affect its optical absorption, charge migration and separation, redox ability, and reaction sites. Therefore, the use of surface defects is valuable for tuning the selectivity and activity of PCN for photocatalytic reactions. For instance, Zhang et al. described a novel one-step KOH-assisted treatment method for the preparation of PCN, in which two types of nitrogen defects (N vacancies and -C≡N groups) were simultaneously introduced into the framework of PCN during the thermal polymerization of urea or

* Corresponding author.

E-mail address: qitao-zhang@szu.edu.cn (Q. Zhang).

¹ These authors contributed equally to this work.

other nitrogen-rich precursors [30]. With an increasing amount of KOH, the light absorption range of the PCN gradually redshifted, which greatly facilitated its photocatalytic H_2 generation capacity. By simply calcining a mixture of PCN and sodium borohydride in an inert atmosphere, Shen et al. simultaneously introduced a boron dopant and $-C\equiv N$ groups defects into PCN [31]. Amino ($-NH_2$) was gradually decomposed and $-C\equiv N$ was introduced by breaking C-N-C bonds, and both the conduction band (CB) and valence band (VB) positions of PCN were continuously tuned and substantially shifted to more positive potentials. Therefore, the band structures of this modified PCN were significantly modulated to achieve effective optical absorption in the visible light range. Thus, the driving force for water oxidation was remarkably enhanced after incorporating the boron dopant and $-C\equiv N$ groups. Yu et al. adopted guanidine hydrochloride (GH) and dicyandiamide (DCD) as precursors to fabricate highly crystalline PCN containing $-C\equiv N$ and $-COOH$ groups by one-step solvothermal method [32]. The enhanced crystallinity and the introduced surface defects in this PCN effectively promoted the photoreduction conversion of CO_2 to hydrocarbon solar fuels while oxidizing water to oxygen. However, in most reported synthesis procedures, $-C\equiv N$ defects are introduced as accompanying defects. The synergistic effects of multiple defects mean that determining the vital role of the cyano group in PCN is extremely elusive. Thus, unraveling the sole role of $-C\equiv N$ defects in cyanided PCN is of great significance for identifying the SAR for H_2O_2 artificial photosynthesis.

In this work, $-C\equiv N$ defects were controllably and solely introduced into the PCN framework by adjusting the thermal condensation temperature and it was determined that the $-C\equiv N$ content was highly correlated with the photocatalytic H_2O_2 evolution activity. Subsequently, a series of advanced spectroscopic characterization techniques (temperature-dependent photoluminescence (TD-PL), scanning Kelvin probe force microscopy (SKPFM), in-situ FT-IR and electron spin resonance (ESR)), density functional theory (DFT) calculations and control experiments were carried out to uncover the $-C\equiv N$ associated SAR of the exciton dissociation energy and efficiency, the surface potential and separation driving force of bound excitons, and the ORR pathway and mechanism of H_2O_2 evolution over the cyanided PCN. The results demonstrate that the introduced $-C\equiv N$ functional groups distinctly accelerated exciton dissociation and charge separation and strengthened the adsorption and activation of O_2 . This provided a driving force for a sequential two-step ORR route: O_2 was first formed via the single-electron reduction of O_2 , then H_2O_2 was produced from the O_2 via the proton-coupled electron transfer (PCET) process. Eventually, the on-site artificial photosynthesized H_2O_2 and O_2 generated by the cyanided PCN led to unexpectedly outstanding performance in removing multifarious environmental persistent organic ECs (4-hydroxybenzoic acid, acetylsalicylic acid, and ibuprofen). 4-Hydroxybenzoic acid is an organic fine chemical that is widely used in the preparation of various dyes, antiseptics, and fungicide color films, and it is also used as a preservative in food, medicine, and cosmetics. Aspirin and ibuprofen are the two best-selling drugs in the world. These drugs are also regarded as typical pharmaceutical and personal care products (PPCPs), and they are also common environmentally persistent organic ECs found in water bodies. This work provides new insights into the $-C\equiv N$ group defect and its associated SAR, inspiring the rational design of other cost-effective functionalized polymeric photocatalysts for hydrogen peroxide artificial photosynthesis and on-site utilization for the removal of environmental persistent organic ECs.

2. Experimental section

2.1. Materials

All reagents used in this work were of analytically pure grade and used without further purification. All aqueous solutions and dispersions were prepared with deionized water. Aladdin Chemistry Co., Ltd. (Shanghai, China) supplied the urea, potassium hydrogen phthalate,

hydrogen chloride, p-benzoquinone (BQ) and potassium chloride. Lactic acid (LA), potassium iodide (KI), ethyl cellulose (EC), silver nitrate ($AgNO_3$), methyl alcohol (MeOH), hydroxybenzoic acid, acetylsalicylic acid and ibuprofen were ordered from Shanghai Macklin Biochemical. Shenzhen Huatepeng Special Gas supplied the oxygen and nitrogen.

2.2. Characterization of photocatalysts

The powder X-ray diffraction (XRD) patterns of the prepared photocatalysts were recorded using Cu $K\alpha$ irradiation (Rigaku, Ultima IV) in the 2θ scanning range of $5-90^\circ$ at a scan rate of 8° min^{-1} with a current of 40 mA and a target voltage of 40 kV. UV-Vis-NIR spectra were collected using a Varian Cary 500 Scan UV-visible system (Agilent). X-ray photoelectron spectroscopy (XPS) experiments were performed on an Escalab 250xi (USA). A Vertex70V spectrometer (Bruker) was used to measure the Fourier transform infrared spectra (FT-IR) of the photocatalysts in the wavenumber range of $400-4000 \text{ cm}^{-1}$. Electron paramagnetic resonance (EPR) spectra were measured with a Bruker A300 at a microwave power level of about 24.6 mW, a temperature of 300 K, and a magnetic field modulation of 9.44 GHz. TD-PL and time-resolved transient photoluminescence (TR-PL) decay spectra were acquired by a HORIBA Fluorolog-3 spectrofluorometer: the photocatalysts were stimulated at 370 nm and the TD-PL spectra of the samples were recorded in the temperature range of 10–300 K under a 450 W xenon lamp. Solid-state ^{13}C nuclear magnetic resonance (NMR) spectra were analyzed using cross-polarization magic-angle spinning (CP-MAS) sequence mode (Advance III HD 400 MHz, Bruker). Carbon dioxide and oxygen temperature-programmed desorption (CO_2/O_2 -TPD) experiments were conducted using a chemisorption analyzer (Micromeritics AutoChem HP 2950). The surface potentials of the photocatalysts were detected by scanning Kelvin probe force microscopy (SKPFM, Bruker Dimension Icon). An SCM-PIT cantilever with a stiffness of 3 N/m was employed to obtain the SKPFM surface potentials with a scan speed of 0.5 Hz. A three-electrode quartz cell with an electrochemical workstation (CHI660E, Chenhua Instruments Co., China) was used to measure the photo-electrochemical characteristics of the photocatalysts.

2.3. Preparation of photocatalysts

In this work, photocatalysts were synthesized by the thermal condensation of urea in a crucible with a cover. To ensure that the ammonolysis reaction sufficiently proceeded during the polymerization to generate PCN, the crucible was tightly wrapped with aluminum foil. A schematic diagram of the synthesis procedures is illustrated in Fig. S1. In a typical process, the optimal catalyst PCN-430 was prepared with urea as the precursor under a static air atmosphere at a thermal polymerization temperature of 430°C . The heating rate was 1°C min^{-1} , and the cooling rate was 5°C min^{-1} . The same process was adopted to prepare other photocatalysts treated at different temperatures of 550, 500, 470, 460, 450, 440, 420, 410, and 400°C . The photocatalysts synthesized at different thermal polymerization temperatures were designated as PCN-T (where T refers to the polymerization temperature). For convenience, the PCN-550, PCN-500, and PCN-430 samples are respectively denoted as N \equiv C-Low, N \equiv C-Mid, and N \equiv C-High in this paper.

2.4. Photocatalytic H_2O_2 production

A multichannel photocatalytic reaction system (PCX50C Discover, Perfect Light Technology Co., Ltd., Beijing, China) with parallel evaluation channels was used to perform photocatalytic H_2O_2 generation reactions in a 60 mL cylindrical quartz bottle with a rubber stopper. The as-prepared photocatalyst (20 mg) in 50 mL of aqueous solution with 10 vol% LA (lactic acid) solution as the hole-trapping agent. The catalyst was ultrasonically dispersed in this solution, followed by oxygenation for about 30 min in the dark to reach O_2 saturation. Subsequently, all bottles were chronologically placed in the reaction system and subjected

to irradiation with visible light ($\lambda \geq 420$ nm, 100 mW cm^{-2}) at 20°C . Iodimetry was used in this study to evaluate H_2O_2 generation, and 3 mL samples of the reaction solution were obtained at hourly intervals. The photocatalysts were filtered using a $0.22 \mu\text{m}$ Millipore filter before H_2O_2 detection. Typically, the resulting solution was mixed with 1 mL of 0.1 mol L^{-1} potassium hydrogen phthalate aqueous solution and 1 mL of 0.4 mol L^{-1} potassium iodide (KI) aqueous solution, then stored in the dark for 1 h. Triiodide anions (I_3^-) were formed in a redox reaction [$\text{H}_2\text{O}_2 + 3\text{I}^- + 2\text{H}^+ \rightarrow \text{I}_3^- + 2\text{H}_2\text{O}$]. The concentration of I_3^- was measured using UV-vis spectroscopy due to its significant absorption at 350 nm, and the concentration of the generated H_2O_2 was calculated according to the calibration curve (Fig. S2). The photocatalytic H_2O_2 production process in pure water was performed using the same procedure without the LA sacrificial agent.

2.5. Photocatalytic ECs degradation performance

The photocatalytic degradation of three model ECs (4-hydroxybenzoic acid: 50 mg L^{-1} , aspirin: 50 mg L^{-1} , ibuprofen: 50 mg L^{-1}) was evaluated under the irradiation of a blue light LED lamp ($\lambda = 420$ nm, 20 mW cm^{-2}) in a 60 mL cylindrical quartz container. High-performance liquid chromatography (HPLC, Agilent 1260 Infinity II) was adopted to determine the PPCPs and intermediate product content. Separation was performed on an EC-C18 column ($4.6 \text{ mm} \times 150 \text{ mm}$, $5 \mu\text{m}$ particle size) at a temperature of about 50°C . 4-Hydroxybenzoic acid, aspirin, and ibuprofen were analyzed using a H_2O -methanol solution (20:80, v/v) at a flow rate of 1 mL min^{-1} as the mobile phase. 4-Hydroxybenzoic acid, aspirin, and ibuprofen were detected at wavelengths of 263 nm, 280 nm, and 260 nm, respectively. The ECs standard curves and degradation curves of 4-hydroxybenzoic acid, aspirin and ibuprofen are provided in Fig.S3.

3. Results and discussion

3.1. Characterization of chemical structure

The thermogravimetric-differential scanning calorimetry analysis (TG-DSC, Fig. S4) of urea shows that the polymerization of urea began at 420°C , indicating that tuning the polymerization temperature would significantly affect the structure of PCN. By varying the thermal polymerization temperature from 400 to 550°C , various PCN-T (T denotes the specific temperature) samples were successfully prepared. All the prepared samples displayed the two characteristic diffractions of PCN centered at $2\theta = 27.6^\circ$ and 13° (Fig. S5). These diffractions were attributed to the interplanar stacking of the conjugated aromatic system and the in-plane repeating units of the continuous heptazine framework, respectively [29,32,35–37]. As shown in FT-IR, (Fig. S6), all the as-prepared samples (with thermal polymerization temperatures above 420°C) contained functional groups representing the fundamental structures of PCN. The characteristic vibration peak located at 809 cm^{-1} was the out-of-plane bending mode of heptazine rings, the absorption bands in the range of $1100\text{--}1750 \text{ cm}^{-1}$ were attributed to the stretching modes of aromatic C-N heterocycles, and the vibrations at about 3200 cm^{-1} were related to the stretching modes of N-H [25,38–40].

Notably, a peak at 2180 cm^{-1} was detected (highlighted by the yellow regions in Fig. S6) when the thermal polymerization temperature was higher than 420°C , which was attributed to the asymmetric stretching vibration of $-\text{C}\equiv\text{N}$ [30–32,38,41]. This peak suggested that $-\text{C}\equiv\text{N}$ groups were successfully introduced into the PCN framework. As shown in Fig. 1a and Fig. 1b, the content of $-\text{C}\equiv\text{N}$ in PCN was strongly correlated with the pyrolysis temperature. The $-\text{C}\equiv\text{N}$ content first increased and then decreased with increasing temperature from 400 to 550°C . Among the as-prepared PCN samples, PCN-430 exhibited the highest $-\text{C}\equiv\text{N}$ group peak intensity, indicating that this sample contained the highest concentration of $-\text{C}\equiv\text{N}$ defects in its PCN framework. The temperature-dependent $-\text{C}\equiv\text{N}$ content of these PCN samples was

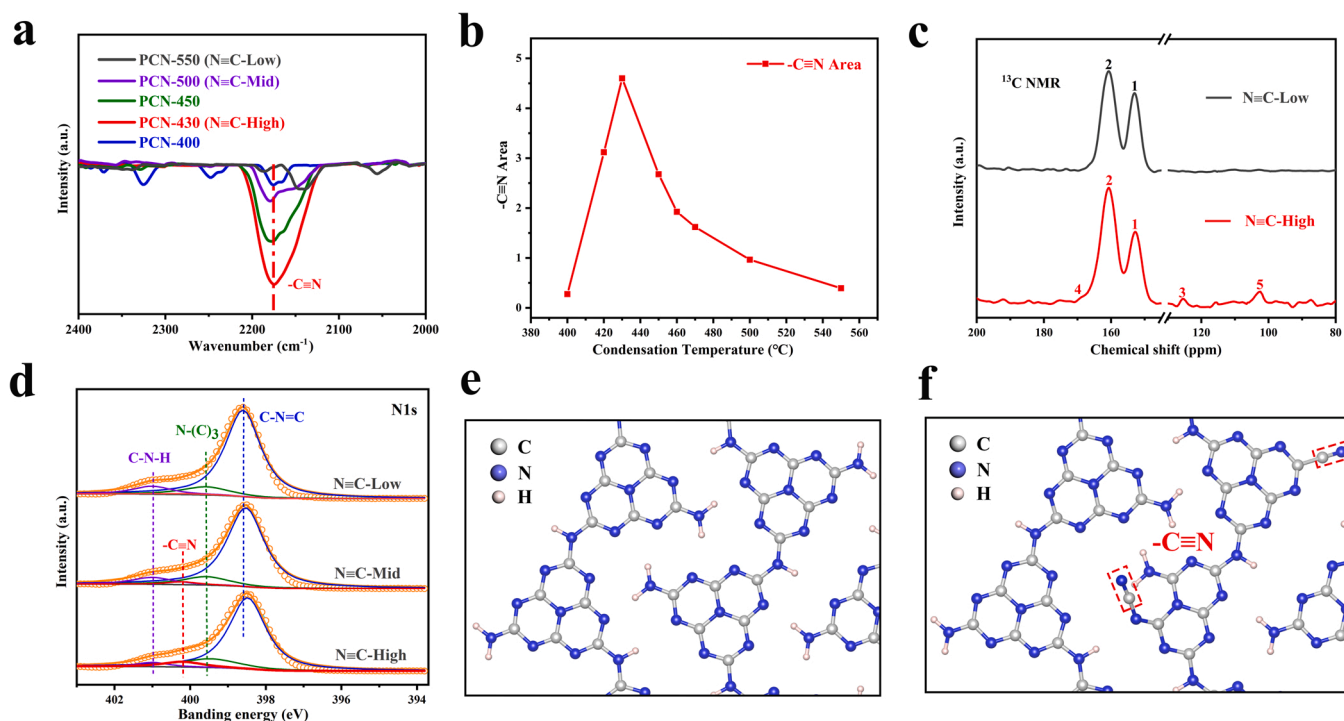


Fig. 1. a) FTIR spectra of the $-\text{C}\equiv\text{N}$ groups of various PCN-T samples; b) Relationship between $-\text{C}\equiv\text{N}$ area and polymerization temperature of PCN (the $-\text{C}\equiv\text{N}$ area was obtained by integrating the FT-IR spectra at 2180 cm^{-1}); c) ^{13}C CP-MAS NMR spectra of $\text{N}\equiv\text{C}$ -Low and $\text{N}\equiv\text{C}$ -High samples; d) High-resolution N 1s XPS spectra of $\text{N}\equiv\text{C}$ -Low, $\text{N}\equiv\text{C}$ -Mid, and $\text{N}\equiv\text{C}$ -High samples; Structure of e) $\text{N}\equiv\text{C}$ -Low sample and f) $\text{N}\equiv\text{C}$ -High sample (the gray, blue, and pink-white balls indicate C, N, and H, respectively).

further demonstrated by solid-state ^{13}C CP-MAS NMR (Fig. 1c) and XPS spectroscopy (Fig. 1d). Fig. 1c shows the solid-state ^{13}C CP-MAS NMR spectra of PCN-550 (also denoted as N≡C-Low) and PCN-430 (also denoted as N≡C-High). Two peaks at 153 and 160.7 ppm corresponded to the characteristic C(1) atoms of $\text{N}=\text{C}-\text{N}_2$ and C(2) atoms of $\text{N}=\text{C}-\text{N}$ ($-\text{NH}_x$) in the heptazine units [18–20,24]. Notably, two new peaks at 123.2 and 169.7 ppm were observed in the N≡C-High spectrum, and these peaks were ascribed to the C(3) atoms in the $-\text{C}\equiv\text{N}$ group defects and the neighboring C(4) atoms, respectively [18,19,31,32]. A new peak was also clearly observed at 102.8 ppm, and this peak was assigned to the C(5) atoms in a pseudo-halogenic cyano group [32] (the positions of C(1), C(2), C(3), C(4) and C(5) are denoted in Fig.S7). This indicates that the introduced $-\text{C}\equiv\text{N}$ group defect might be generated from the partial conversion of $\text{N}=\text{C}-\text{N}_2$ units. Moreover, the high-resolution C 1 s XPS spectra of all the prepared samples (Fig. S8) showed two typical peaks near 284.6 and 288.2 eV, corresponding to the C-C bond of adventitious hydrocarbons and $\text{N}=\text{C}-\text{N}$ coordination in the framework of PCN, respectively [27,28,33]. The high-resolution N 1 s spectra (Fig. 1d) of the obtained samples displayed three typical peaks near 398.6, 399.6 and 401 eV corresponding to $\text{C}=\text{N}-\text{C}$, $\text{N}-(\text{C})_3$ and $\text{N}-\text{H}$ species in the PCN framework, respectively [24,34,35]. Notably, two new peaks were visible at 286.2 eV (C 1 s XPS) and 400.2 eV (N 1 s) for N≡C-High and N≡C-Mid, which was ascribed to the $-\text{C}\equiv\text{N}$ group [18,20,29]. The

proportions of the $-\text{C}\equiv\text{N}$ peak area in the high-resolution C 1 s and N 1 s XPS spectra of N≡C-Low, N≡C-Mid, and N≡C-High are given in Table S1. Considering that PCN-420 and PCN-440 exhibit similar phase structures compared to that of PCN-430 (also denoted as N≡C-High), the XRD, XPS, FT-IR, solid-state ^{13}C NMR, photocurrent intensity, electrochemical impedance spectra (EIS), steady-state photoluminescence (PL), TR-PL measurements and corresponding H_2O_2 photosynthesis performance tests of PCN-420 and PCN-440 are presented in Fig. S9 to support the choice of PCN-430 as the N≡C-High sample. Therefore, N≡C-High can be regarded as a $-\text{C}\equiv\text{N}$ defect-rich PCN sample, while N≡C-Mid and N≡C-Low contain medium and low amounts of $-\text{C}\equiv\text{N}$, respectively. The following study of the SAR focuses on these three PCN samples with varying $-\text{C}\equiv\text{N}$ content.

3.2. Photocatalytic H_2O_2 generation performance

The effect of $-\text{C}\equiv\text{N}$ content on the artificial photosynthesis of H_2O_2 over the prepared samples via O_2 photoreduction was systematically investigated under visible-light irradiation. Fig. 2a, Fig. S10 and Fig.S11 show that with or without a sacrificial agent, the concentrations of generated H_2O_2 linearly increased over time. Considering that LA is a common domestic pollutant and has the outstanding property of consuming holes, LA was selected as the sacrificial agent during H_2O_2

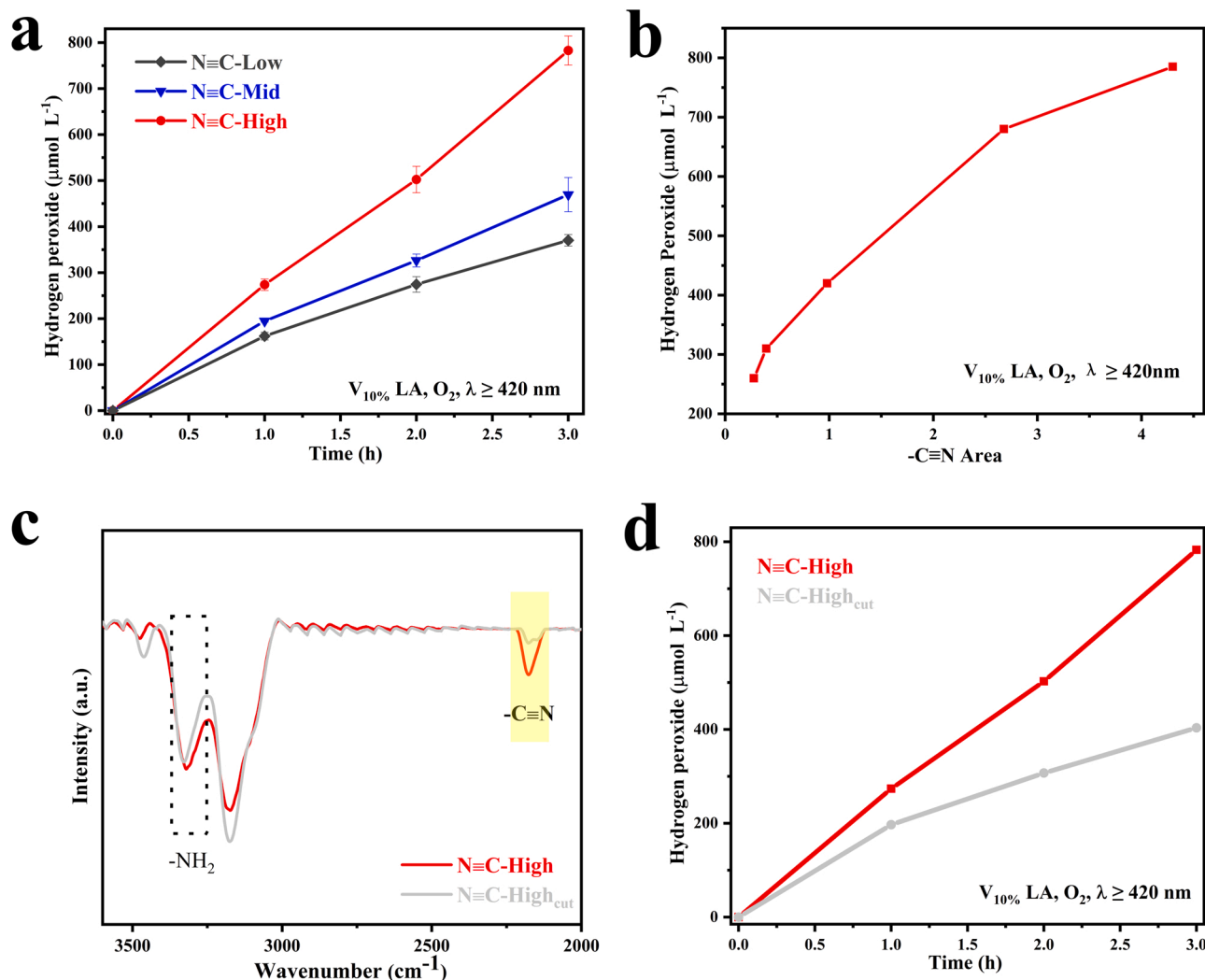


Fig. 2. a) H_2O_2 yield vs. time of N≡C-High, N≡C-Mid, and N≡C-Low ($\lambda \geq 420 \text{ nm}$, 20 mg catalyst in 50 mL solution, 10 vol% lactic acid, and O_2 saturation for 30 min); b) H_2O_2 yield vs. $-\text{C}\equiv\text{N}$ group content (the $-\text{C}\equiv\text{N}$ area was calculated by integrating the FT-IR spectra at 2180 cm^{-1}); c) FT-IR spectra and d) H_2O_2 yield curves of N≡C-High and N≡C-High_{cut} ("cut" denotes the sample where the $-\text{C}\equiv\text{N}$ group was quenched).

photosynthesis. The performances of this photocatalytic system using other common sacrificial agents (methanol, ethanol, and isopropyl alcohol) are reported in Fig. S11. Among the samples, N≡C-High exhibited the highest photoactivity. The performance of N≡C-High was significantly better than that of N≡C-Mid, N≡C-Low, and the other catalysts (Fig. 2b and Fig. S12). This indicated the critical roles of -C≡N defects in promoting H₂O₂ artificial photosynthesis. The apparent quantum yield (AQY) of N≡C-High at 420 nm (4.58%) was about two times higher than that of N≡C-Low (2.48%) (Table S2). The photocatalytic H₂O₂ production activity of N≡C-High demonstrates its outstanding performance compared with other reported metal-free PCN photocatalysts (Table S3). Moreover, when the -C≡N area was correlated with the H₂O₂ evolution yield, a positive correlation was observed between the -C≡N group concentration and photocatalytic activity (Fig. 2b and Fig. S12), further demonstrating that the photoreduction activity of O₂ to H₂O₂ was significantly related to the introduced -C≡N content. To further determine the role of the -C≡N group, it is necessary to clarify the effects of -NH_x groups and structural defects (Fig. S7). Thus, EPR and CO₂-TPD experiments were performed with N≡C-High, N≡C-Mid, N≡C-Low and N≡C-High_{cut} to determine the content of -NH_x groups and the structural defects in these catalysts (Fig. S13) [42–44]. Interestingly, after -C≡N group quenching, the structural defects and -NH_x groups increased, but the photocatalytic performance dramatically decreased (Fig. 2c–d). This indicated that the structural defect content and -NH_x group content of the photocatalysts (N≡C-High, N≡C-Mid, N≡C-Low, and N≡C-High_{cut}) did not significantly contribute to their photocatalytic H₂O₂ generation performance (Fig. S12 and Fig. S13). These phenomena further explained the key role of the -C≡N group in promoting the performance of the catalysts for H₂O₂ artificial photosynthesis. The reusability and stability of N≡C-High were also systematically studied. As shown in Fig. S14, after five reaction cycles, the photocatalytic performance of N≡C-High did not significantly change, and XRD patterns and FT-IR spectra obtained before and after the reaction also negligibly changed. These results indicate that the N≡C-High photocatalyst has good reusability and stability.

3.3. Structure-activity relationship and on-site application

3.3.1. Effects of -C≡N on charge separation

To further investigate the mechanism of the introduced -C≡N group driving photocatalytic H₂O₂ evolution, the effects of -C≡N on the light absorption behavior, band structure, charge transfer properties, and the adsorption of reactants were systematically studied. The specific surface area was first investigated because the specific surface areas of photocatalysts significantly affect their photocatalytic activity. Intriguingly, the introduction of the -C≡N group defect led to a decline in specific surface area (Figs. S15–S16 and Table S4). Thus, the N≡C-High catalyst, which displayed the best photocatalytic activity, did not have the highest surface area, indicating that the surface area might not be the key factor determining the photocatalytic activity in this study. Based on their UV-Vis diffuse reflectance spectra (DRS, Fig. S17) and Mott-Schottky measurements (Fig. S18a–c), the slight variations in the band alignments of N≡C-Low, N≡C-Mid, and N≡C-High were compared (Fig. S18d) [45]. This comparison indicated that the CB and VB positions of the cyanided PCN were slightly affected by the pyrolysis temperature, and this was further demonstrated by DFT calculations (Fig. S19), which indicated that some impurity mid-gap energy levels were introduced.

In addition to the mid-gap energy levels, the -C≡N group defects were also expected to significantly influence the separation and transport of charge carriers [30,31]. Therefore, transient photocurrent response curves, EIS, steady-state PL, TR-PL, and exciton dissociation energy values were also obtained to explore the impact of the -C≡N group on the charge transfer dynamics of the as-prepared photocatalysts. The transient photo-current responses of N≡C-High exhibited a photo-current intensity about two times higher than that of N≡C-Low,

as depicted in Fig. 3a. The EIS radius of N≡C-High was smaller than that of the other samples (Fig. 3b), and N≡C-High also exhibited a weaker fluorescence signal intensity compared to N≡C-Low and N≡C-Mid (Fig. 3c). This indicated that the -C≡N group defects endowed N≡C-High with lower electron transfer resistance. As is well known, more effective charge separation and migration lead to a lower probability of charge carrier recombination [46,47]. As shown in Fig. 3d, TR-PL analysis indicated that N≡C-High, N≡C-Mid, and N≡C-Low had average fluorescence lifetimes (τ_n) of 7.63, 5.75, and 5.15 ns. This suggested that N≡C-High was able to photogenerate electrons with longer lifetimes to participate in the activation and reduction of O₂ to produce H₂O₂ compared to the other samples. This was because the Frenkel exciton binding effect typically influences organic semiconductors, meaning that polymeric PCN photocatalysts usually exhibit sluggish carrier dynamics. The exciton binding energy of electrons and holes under the Coulomb force of the cyanided PCN samples was further investigated via TD-PL, (Fig. 3e) using the equation " $I(T) = I_0/(1 + Ae^{-\frac{E_b}{k_B T}})$ ", where I_0 is the PL intensity at 0 K, k_B is the Boltzmann constant, and E_b is the binding energy of an exciton [48,49]. As displayed in Fig. 3f, the E_b values of N≡C-High and N≡C-Low were calculated to be 32.05 and 51.96 meV, respectively. The exciton dissociation efficiencies (EDE) of these samples were calculated to be 27.75% and 12.51% according to the equation " $EDE = e^{-E_b/(k_B T)}$ " ($k_B T \approx 25$ meV at room temperature) [48,49]. This demonstrates the much higher electron-hole separation efficiency of N≡C-High compared to that of N≡C-Low. This calculation is in good agreement with the photocurrent intensity, EIS, PL, TR-PL, and photocatalytic activity analysis. To further illustrate the intrinsic connection between the -C≡N group content and the charge separation dynamics of these catalysts, first-principles calculations were adopted to simulate the corresponding charge density distributions of the highest occupied molecular orbital (HOMO) and the lowest unoccupied molecular orbital (LUMO) in the energy band structure of N≡C-Low and N≡C-High. As shown in Fig. 3g, the charge density distributions at the HOMO and LUMO of N≡C-Low were extremely uniform, indicating the overlapping of electrons and holes. In contrast, the HOMO and LUMO in N≡C-High were significantly delocalized (Fig. 3h), showing the effective spatial separation of electron-hole pairs. More importantly, the spatial separation of the charge carriers in the HOMO and LUMO in N≡C-High guaranteed that the redox sites in this catalyst were separated, inhibiting undesirable reverse reactions or charge carrier recombination. This was desirable for enabling the electrons and holes to undergo catalytic reactions at the catalyst surface. As shown in Fig. S20, the electrostatic potential (ESP) distributions of N≡C-Low and N≡C-High further demonstrated that the introduction of polarized -C≡N functional groups broke the structural symmetry of the PCN framework, which significantly increased the concentration of accessible redox reaction sites. Therefore, the separation and transport of charge carriers was facilitated in the cyanided PCN photocatalyst, which was conducive to driving the photocatalytic reaction. SKPFM was used to directly determine the spatial separation of charges in the cyanided PCN. The N≡C-High sample had a surface photovoltage (SPV, $SPV = CPD_{light} - CPD_{dark}$) 6.4 times higher than that of N≡C-Low after visible light irradiation. This indicated that the built-in electric field (BIEF) of the N≡C-High photocatalyst was greatly enhanced by the polarization effect of the -C≡N functional group (Fig. 4). Thus, this analysis establishes the SAR between the -C≡N group defects in the cyanided; and its synergistic mechanism for charge separation.

3.3.2. Effects of -C≡N on oxygen activation

Typically, oxygen molecules can be reduced to H₂O₂ through a direct/indirect two-electron process or reduced to H₂O via a four-electron pathway. Our previous studies revealed that introducing single Sb metal sites or a barbituric acid comonomer in the PCN framework played a vital role in influencing selectivity for the two-electron oxygen reduction reaction (2e⁻ ORR) to promote the production of H₂O₂ and

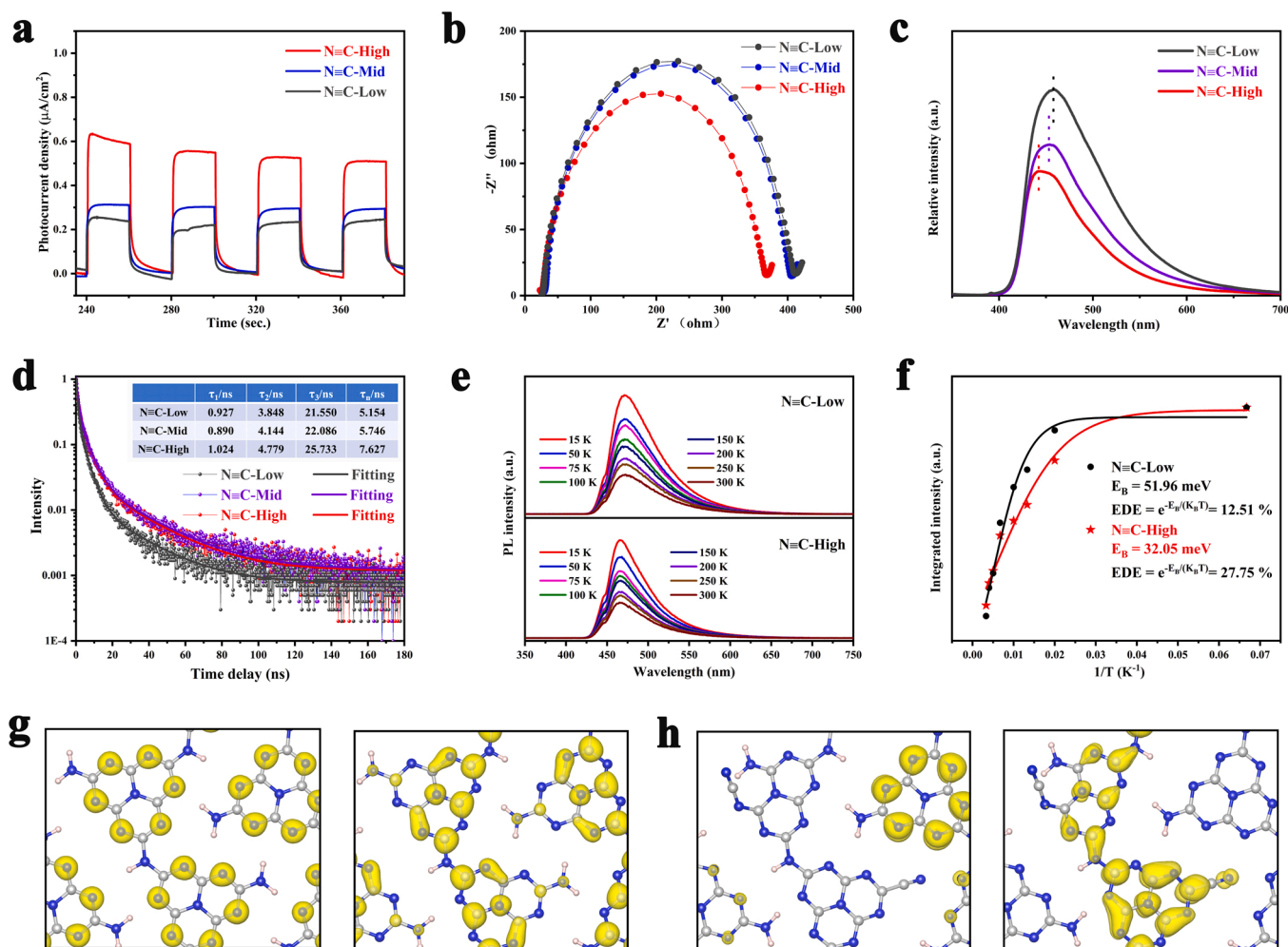


Fig. 3. a) Photocurrent intensity curves, b) electrochemical impedance spectra (EIS), c) steady-state photoluminescence spectra, and d) time-resolved photoluminescence spectra of N≡C-Low, N≡C-Mid, and N≡C-High; e) Temperature-dependent PL (TD-PL) spectra of N≡C-Low and N≡C-High in the range of 15–300 K under 320 nm laser excitation; f) Integrated PL emission intensities of N≡C-Low and N≡C-High as a function of temperature from 15 K to 300 K; g, h) HOMO and LUMO distributions of N≡C-Low (g) and N≡C-High (h). The gray, blue, and pink-white spheres denote C, N, and H atoms, respectively.

accumulate photogenerated electrons for O_2 activation [1,50]. In this work, the interaction between the $-\text{C}\equiv\text{N}$ group and O_2 in the photocatalytic system was investigated by performing O_2 -TPD (Fig. S21). The O_2 adsorption capacity of N≡C-High was much higher than that of N≡C-Low. Therefore, the separation and transport of charge carriers was facilitated by $\text{C}\equiv\text{N}$ active sites, and the presence of these sites was conducive to enabling a higher ORR rate to produce H_2O_2 . The average electron transfer number (n) is an important index for evaluating the selectivity of O_2 activation. Fig. S22 shows the linear sweep voltammetry (LSV) curves of the as-prepared photocatalysts, which were obtained using a conducting rotating disk glassy carbon electrode (RDE) in O_2 saturated 0.1 M KOH at different rotating speeds. The corresponding electron transfer numbers were then obtained (Fig. 5a). The n value of N≡C-High was 2.358, while those of N≡C-Mid and N≡C-Low were 2.681 and 2.847, respectively. Therefore, O_2 activation by N≡C-High was more selective toward the two-electron transfer pathway. This demonstrated that the $-\text{C}\equiv\text{N}$ group in the cyanided PCN was conducive to driving oxygen activation toward the $2e^-$ ORR pathway.

To better reveal the detailed H_2O_2 formation pathways and understand the O_2 activation mechanism, various control experiments were conducted with sacrificial agents. AgNO_3 and p-BQ were used as electron (e) and superoxide radical ($\cdot\text{O}_2^-$) scavengers, respectively [1,2,8,51]. As shown in Fig. 5b, when O_2 was replaced by air, the H_2O_2 yield was reduced by about a quarter. When the O_2 was replaced with N_2 ,

almost no H_2O_2 was detected. This suggested that photocatalytic H_2O_2 evolution did not occur without the presence of O_2 as a reactant, and that the oxygen reduction pathway was the main route to the photosynthesis of H_2O_2 in this study. When electron scavengers (AgNO_3) were added into the reaction system to remove the photogenerated electrons, H_2O_2 was barely detected, further demonstrating that the photocatalytic H_2O_2 evolution mainly proceeded through the ORR pathway rather than the water oxidation reaction (WOR). When BQ was used to eliminate O_2^- species, the H_2O_2 yield significantly declined, a further demonstration of the indirect $2e^-$ ORR pathway. This result also demonstrated that O_2^- was a vital intermediate during H_2O_2 artificial photosynthesis. To gain deeper insights into the reaction path, in situ FT-IR spectroscopy and in situ EPR analysis were carried out. For the in-situ FT-IR analysis, the cyanided PCN sample was held in the dark for 30 min before light irradiation to allow the methyl alcohol and water to reach adsorption-desorption equilibrium on the sample surface. After 30 min (Fig. S23), the PCN background was subtracted, allowing the formation of surface functional groups to be observed [52,53]. The FT-IR adsorption experimental results of N≡C-High with CH_3OH , H_2O and H_2O_2 are also presented in Fig. S24, to further illustrate the accuracy of in situ FT-IR. As shown in Fig. 5c, visible light irradiation induced the emergence of several new peaks. The bands at $990\text{--}1030 \text{ cm}^{-1}$ and $1270\text{--}1320 \text{ cm}^{-1}$ were assigned to the O-O stretching modes of surface-adsorbed O_2 [52,54–56] and surface-adsorbed superoxide

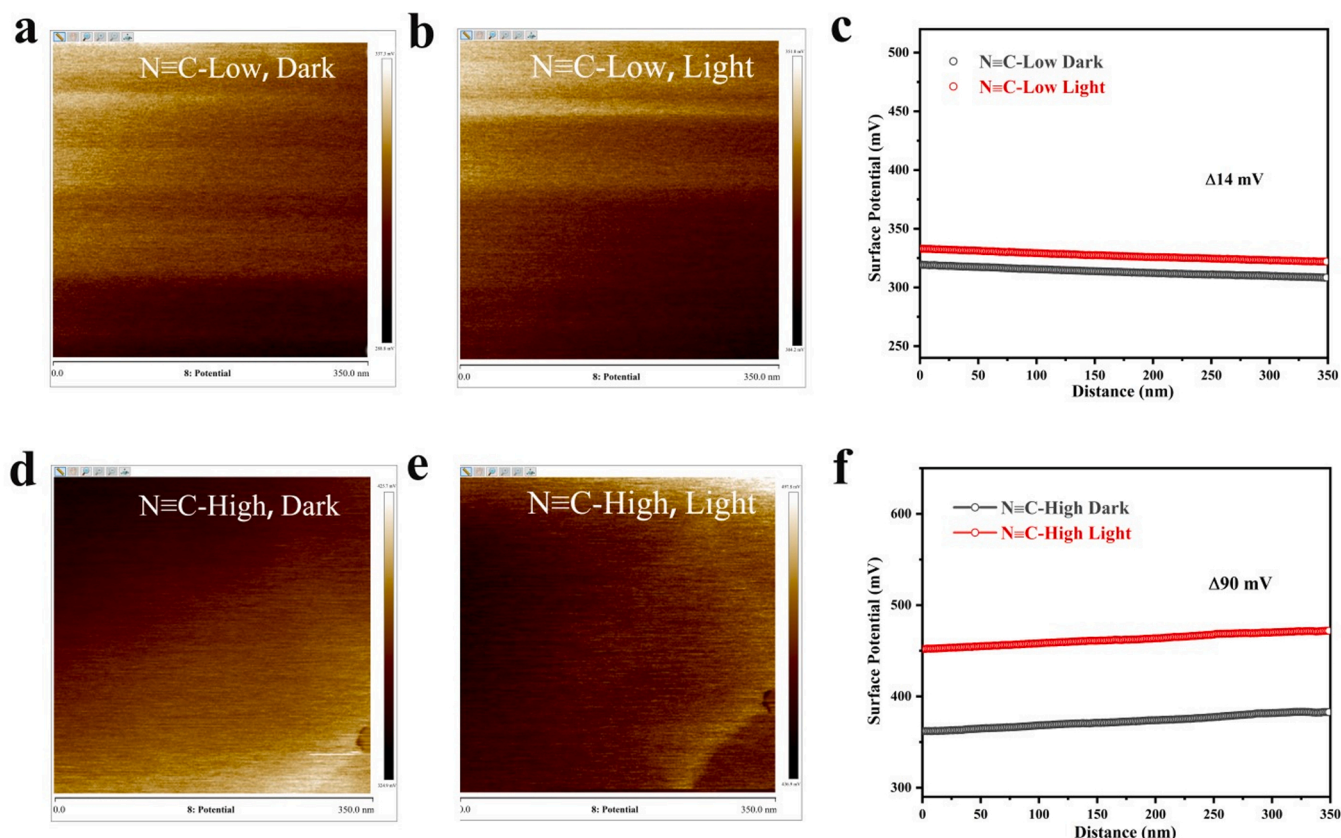


Fig. 4. SKPFM surface potential images of N≡C-Low in the dark (a) and under light (b), N≡C-High in the dark (d) and under light (e) Surface potential difference curves of N≡C-Low (c) and N≡C-High (f).

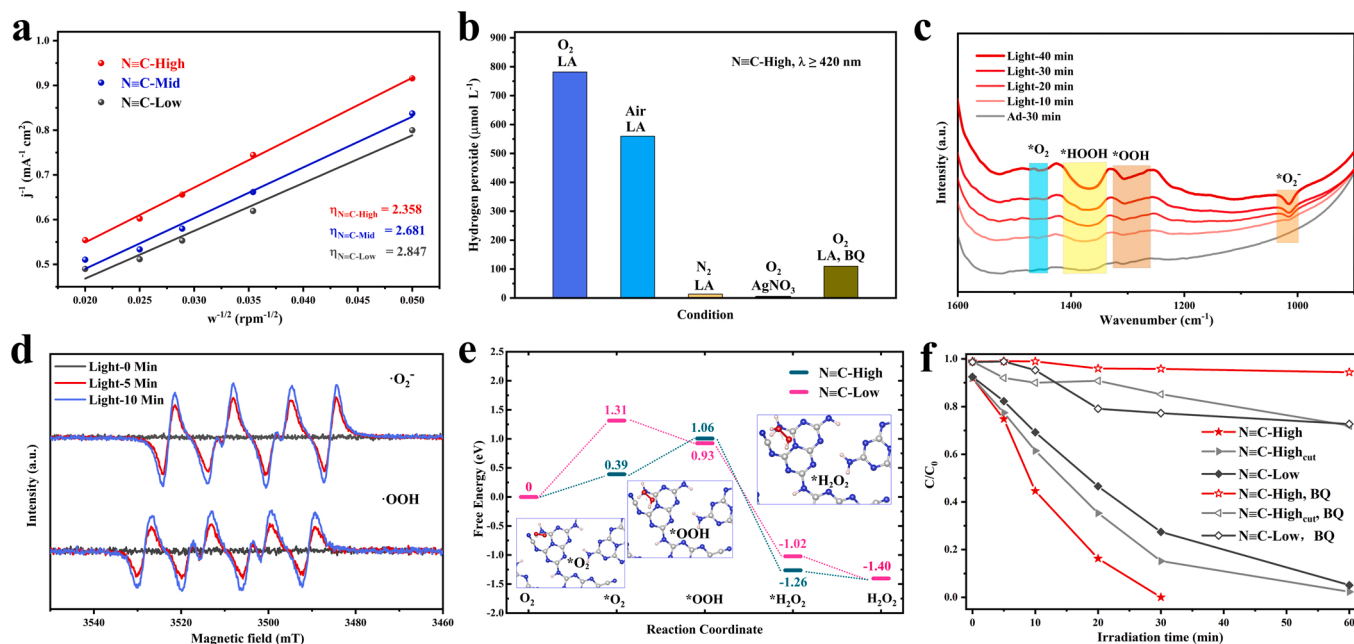


Fig. 5. a) Koutecky-Levich plots of N≡C-Low, N≡C-Mid, and N≡C-High; b) photocatalytic H_2O_2 generation rates of N≡C-High under different reaction conditions ($\lambda \geq 420$ nm, 100 mW cm^{-2} ; 20 mg catalyst in 50 mL solution); c) in situ FT-IR spectra of N≡C-High with increasing irradiation time; d) in situ EPR signals of O_2 and OOH over N≡C-High in the presence of DMPO; e) Gibbs free energy calculations for H_2O_2 production by N≡C-High and N≡C-Low; f) photocatalytic ECs (4-hydroxybenzoic acid) removal performance ($\lambda = 420$ nm) of various PCN samples.

(*OOH) [53,54,57], respectively. The vibration bands at $1340\text{--}1405 \text{ cm}^{-1}$ and $1440\text{--}1470 \text{ cm}^{-1}$ were attributed to the OOH bending mode of surface-adsorbed hydroperoxide (H_2O_2) [54,57] and

adsorbed molecular oxygen (O_2) [54,56]. Notably, with the extension of visible light irradiation, the O-O stretching modes of surface-adsorbed O_2 , O_2^* , OOH and the OOH bending modes of surface-adsorbed H_2O_2

gradually increased in intensity, implying the sustainable formation of these intermediate ROS. This was further indicated by in situ EPR characterization (Fig. 5d). No radical signals of $\cdot\text{O}_2$ and $\cdot\text{OOH}$ were observed without visible light irradiation, but after 10 min of irradiation, the $\cdot\text{O}_2$ and $\cdot\text{OOH}$ signals were clearly observed. This was a further demonstration that the photocatalytic H_2O_2 evolution of N≡C-High was mainly driven by the indirect $2e^-$ ORR and that $\cdot\text{O}_2$ and $\cdot\text{OOH}$ radicals were vital ROS intermediates for photocatalytic H_2O_2 evolution, corroborating the active species trapping experimental results [1,8,58]. Thus, the photocatalytic evolution of H_2O_2 over the cyanided PCN followed the indirect $2e^-$ ORR pathway (also known as the two-step single electron process). Specifically, O_2 was first reduced by one electron to $\cdot\text{O}_2$, and the obtained $\cdot\text{O}_2$ species was involved in the following PCET processes to produce H_2O_2 : $[\text{O}_2 + e^- \rightarrow \cdot\text{O}_2, \cdot\text{O}_2 + \text{H}^+ + e^- \rightarrow \cdot\text{OOH}, \cdot\text{OOH} + \text{H}^+ \rightarrow \text{H}_2\text{O}_2]$.

To investigate why the $-\text{C}\equiv\text{N}$ group was able to facilitate O_2 activation with high selectivity for $2e^-$ ORR, the free energies of various reaction pathways for H_2O_2 generation were simulated by DFT calculations (Fig. 5e). Two PCN models (with and without a $-\text{C}\equiv\text{N}$ group) were established and optimized (Fig. S25), simulating N≡C-Low and N≡C-High, respectively. In good agreement with the O_2 -TPD results (Fig. S21), the O_2 adsorption energy of N≡C-High (0.39 eV) was significantly lower than that of N≡C-Low (1.31 eV), indicating that the presence of the $-\text{C}\equiv\text{N}$ group facilitated the adsorption of O_2 for the subsequent reaction. The Gibbs free energy from $[\text{O}_2 + \text{H}^+ + e^- + *]$ to $*\text{OOH}$ of N≡C-High (1.06 eV) was very close to that of N≡C-Low (0.93 eV), while the energy of formation for transforming $*\text{OOH}$ to $*\text{H}_2\text{O}_2$ of N≡C-High (2.32 eV) was much higher than that of N≡C-Low (1.95 eV). This implies that the $-\text{C}\equiv\text{N}$ group defect enabled N≡C-High to efficiently adsorb and activate O_2 on its functional group polarized surface, leading to a significantly higher abundance of $*\text{O}_2$. The $-\text{C}\equiv\text{N}$ group also facilitated the hydrogenation of $*\text{OOH}$ to $*\text{H}_2\text{O}_2$, and the desorption of $*\text{H}_2\text{O}_2$. Thus, the cyanided PCN fabricated in this study is an outstanding candidate photocatalyst for driving H_2O_2 artificial photosynthesis, and the abundance of ROS radicals generated during the indirect $2e^-$ ORR is eminently suitable for the on-site removal of emerging contaminants (ECs) to achieve sustainable water purification.

3.3.3. On-site utilization for emerging contaminants removal

According to the above analysis, introducing the $-\text{C}\equiv\text{N}$ group into the PCN photocatalyst can reduce the exciton binding energy of electrons and holes, promote the adsorption and activation of O_2 , and boost the generation of abundant ROS during photocatalytic H_2O_2 generation. If these in-situ generated highly reactive radicals could be utilized on-site for environmental purification applications, this would be highly meaningful for the development of a sustainable society. Ubiquitous ECs have been detected in drinking water, groundwater, and urban waste leachate. It has been reported that long-term exposure to low concentrations of a variety of pharmaceutical compounds and ECs seriously disturbs entire ecosystems and affects the health of plants, animals, and humans. Thus, the feasibility of using this metal-free photocatalyst for the removal of ECs in water was investigated.

In this study, three representative ECs (4-hydroxybenzoic acid, aspirin, and ibuprofen) were adopted as water body model pollutants to evaluate the performance and general applicability of the as-prepared cyanided PCN. Photocatalytic removal of ECs was performed under 420 nm LED light irradiation, and the 4-hydroxybenzoic acid photocatalytic degradation performance of N≡C-High was also evaluated under visible light and simulated sunlight sources (Fig. S26). As shown in Fig. 5f, Fig. S3c, and Fig. S27, N≡C-High exhibited much better degradation performance than N≡C-Low and N≡C-High_{cut}, fully degrading 50 mg L⁻¹ of ECs within 60 min. Using the removal of 4-hydroxybenzoic acid as an example, BQ radical capture experiments and EPR measurements were carried out to probe the main ROS species involved in the photocatalytic removal of 4-hydroxybenzoic acid (Fig. 5f and Fig. S28). The results indicated that $\cdot\text{O}_2$ and hydroxyl radical ($\cdot\text{OH}$)

ROS both played vital roles in driving the on-site degradation of this EC. The $\cdot\text{O}_2$ radicals were derived from single-electron ORR during the indirect $2e^-$ ORR, while the $\cdot\text{OH}$ radicals were mainly generated by H_2O_2 capturing photogenerated electrons, allowing a disproportionation reaction to occur [59] (The potential of one-electron water oxidation to produce $\cdot\text{OH}$ radicals is +2.32 V vs. NHE [60–62], which is much larger than VB potential of N≡C-High. Thus, it is thermodynamically difficult for this reaction to occur in this experiment.) In addition, to prove that $\cdot\text{OH}$ radicals were mainly generated by H_2O_2 , EPR spectra of the N≡C-High photocatalyst were obtained with or without additional H_2O_2 in solution, as shown in Fig. S29a. Under visible light irradiation, the $\cdot\text{OH}$ signal intensity was greatly strengthened owing to H_2O_2 photolysis by the N≡C-High photocatalyst. Control experiments of the photocatalytic degradation of ECs with additional H_2O_2 under dark/-light irradiation were also carried out. As shown in Fig. S29b, ECs were degraded by about 40% within 140 min under light, N_2 , and 40 μL H_2O_2 (30 wt%). However, negligible EC degradation occurred in the dark. Thus, the above-mentioned results demonstrate that $\cdot\text{OH}$ was mainly derived from H_2O_2 and that this ROS played an important role in the photocatalytic removal of ECs. A schematic diagram illustrating the EC degradation process is displayed in Fig. 6. The introduction of the $-\text{C}\equiv\text{N}$ group in the PCN framework leads to the significant generation of ROS during $2e^-$ ORR, which remarkably promotes the removal of various ECs.

4. Conclusion

In summary, we fabricated a series of metal-free PCN photocatalysts with varying $-\text{C}\equiv\text{N}$ group content by adjusting the thermal condensation temperature. Interestingly, the $-\text{C}\equiv\text{N}$ content in the PCN was temperature-dependent and positively related to photocatalytic H_2O_2 production activity. Both experimental and theoretical analysis established the SAR between the $-\text{C}\equiv\text{N}$ group defect in the cyanided PCN and its synergistic mechanism for exciton dissociation, charge separation, oxygen activation, and indirect $2e^-$ ORR to produce H_2O_2 with excellent performance and high selectivity. The in-situ generation of a large amount of ROS during H_2O_2 artificial photosynthesis significantly promoted the removal of various ECs, including 4-hydroxybenzoic acid, aspirin, and ibuprofen. This study provides new insights into the roles of the $-\text{C}\equiv\text{N}$ group in PCN and deepens the theoretical understanding of utilizing defects for designing PCN-based catalysts. The use of $-\text{C}\equiv\text{N}$ functionalized PCN to drive H_2O_2 artificial photosynthesis and on-site utilization in this work is expected to provide guidance for fabricating other cost-effective metal-free polymeric photocatalysts for environmental remediation and energy-related applications.

CRedit authorship contribution statement

Yunfei Ma: Methodology, Validation, Formal analysis, Investigation, Data curation, Writing – original draft. **Hongli Sun:** Methodology, Validation, Formal analysis, Investigation, Data curation, Writing – original draft. **Qizhen Wang:** Experimental Measurements, Software. **Like Sun:** Experimental Measurements, Software. **Zailun Liu:** Data collection and processing, Discussion. **Yao Xie:** Data collection and processing, Discussion. **Qitao Zhang:** Supervision, Conceptualization, Discussion, Writing – review & editing. **Chenliang Su:** Supervision, Conceptualization, Discussion, Writing – review & editing. **Dianyuan Fan:** Resources, Supervision.

Declaration of Competing Interest

The authors declare that they have no known competing financial interests or personal relationships that could have appeared to influence the work reported in this paper.

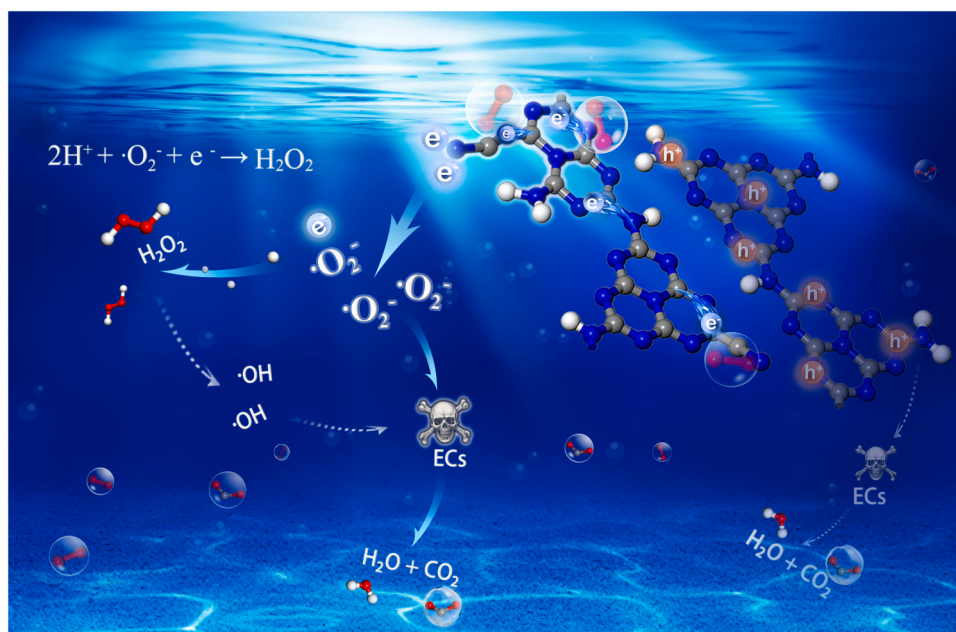


Fig. 6. Schematic diagram of the ROS related to the $-\text{C}\equiv\text{N}$ group defect in the cyanided PCN promoting the photocatalytic degradation of emerging contaminants (ECs). The blue, gray, white and red spheres represent N, C, H and O atoms, respectively.

Data Availability

Data will be made available on request.

Acknowledgements

The authors acknowledge the financial support of the National Natural Science Foundation of China (Nos. 22102102, 21972094, 21805191), Guangdong Basic and Applied Basic Research Foundation (2020A1515010982), Shenzhen Science and Technology Program (Nos. 20190808142001745, 20200812122947002, 20200812160737002, 20200714114434086), China Postdoctoral Science Foundation (2021T140472), Shenzhen Peacock Plan (Nos. 20210308299C, 20210802524B, 20180921273B) and Graduate Innovation and Development Fund project of Shenzhen University (No. 315-000047060). The authors thank Dr. Nan Jian from the Electron Microscope Center of Shenzhen University for his help with HR-TEM measurement.

Appendix A. Supporting information

Supplementary data associated with this article can be found in the online version at [doi:10.1016/j.apcatb.2023.122878](https://doi.org/10.1016/j.apcatb.2023.122878).

References

- [1] Z. Teng, Q. Zhang, H. Yang, K. Kato, W. Yang, Y.-R. Lu, S. Liu, C. Wang, A. Yamakata, C. Su, B. Liu, T. Ohno, Atomically dispersed antimony on carbon nitride for the artificial photosynthesis of hydrogen peroxide, *Nat. Catalysis* 4 (2021) 374–384.
- [2] X. Zhang, P. Ma, C. Wang, L. Gan, X. Chen, P. Zhang, Y. Wang, H. Li, L. Wang, X. Zhou, K. Zheng, Unraveling the dual defect sites in graphite carbon nitride for ultra-high photocatalytic H_2O_2 evolution, *Energy Environ. Sci.* 15 (2022) 830–842.
- [3] Z. Teng, W. Caia, W. Sima, Q. Zhang, C. Wang, C. Su, T. Ohno, Photoexcited single metal atom catalysts for heterogeneous photocatalytic H_2O_2 production: Pragmatic guidelines for predicting charge separation, *Appl. Catal. B: Environ.* 282 (2021), 119589.
- [4] H. Huang, Q. Zhang, R. Shi, C. Su, Y. Wang, J. Zhao, T. Zhang, Synergistic effect of triphase interface and fluid control for efficient photosynthesis of residue-free H_2O_2 , *Appl. Catal. B: Environ.* 317 (2022), 121731.
- [5] J.M. Campos-Martin, G. Blanco-Brieva, J.L. Fierro, Hydrogen peroxide synthesis: an outlook beyond the anthraquinone process, *Angew. Chem. Int. Ed.* 45 (2006) 6962–6984.
- [6] Y. Jiang, P. Ni, C. Chen, Y. Lu, P. Yang, B. Kong, A. Fisher, X. Wang, Selective electrochemical H_2O_2 production through two-electron oxygen electrochemistry, *Adv. Energy Mater.* 8 (2018) 1801909.
- [7] C. Feng, L. Tang, Y. Deng, J. Wang, J. Luo, Y. Liu, X. Ouyang, H. Yang, J. Yu, J. Wang, Synthesis of Leaf-Vein-Like g- C_3N_4 with tunable band structures and charge transfer properties for selective photocatalytic H_2O_2 evolution, *Adv. Funct. Mater.* 30 (2020) 2001922.
- [8] H. Che, X. Gao, J. Chen, J. Hou, Y. Ao, P. Wang, Iodide-Induced fragmentation of polymerized hydrophilic carbon nitride for high-performance quasi-homogeneous photocatalytic H_2O_2 production, *Angew. Chem. Int. Ed.* 60 (2021) 25546–25550.
- [9] H. Sun, W. Ou, L. Sun, B. Wang, C. Su, Recent advances in nature-inspired nanocatalytic reduction of organic molecules with water, *Nano Res.* 15 (2022) 10292–10315.
- [10] W.J. Ong, L.L. Tan, Y.H. Ng, S.T. Yong, S.P. Chai, Graphitic carbon nitride (g- C_3N_4)-Based photocatalysts for artificial photosynthesis and environmental remediation: are we a step closer to achieving sustainability? *Chem. Rev.* 116 (2016) 7159–7329.
- [11] Z. Liu, L. Sun, Q. Zhang, Z. Teng, H. Sun, C. Su, TiO_2 -supported single-atom catalysts: synthesis, structure, and application, *Chem. Res. Chin. Univ.* 38 (2022) 1123–1138.
- [12] Y. Xing, X. Wang, S. Hao, X. Zhang, X. Wang, W. Ma, G. Zhao, X. Xu, Recent advances in the improvement of g- C_3N_4 based photocatalytic materials, *Chin. Chem. Lett.* 32 (2021) 13–20.
- [13] H. Sun, Y. Ma, Q. Zhang, C. Su, Engineering the local coordination environment of single-atom catalysts and their applications in photocatalytic water splitting: a review, *Trans. Tianjin Univ.* 27 (2021) 313–330.
- [14] L. Li, I.Mu Hasan, Farwa, R. He, L. Peng, N. Xu, N.K. Niazi, J.-N. Zhang, J. Qiao, Copper as a single metal atom based photo-, electro-, and photoelectrochemical catalyst decorated on carbon nitride surface for efficient CO_2 reduction: a review, *Nano Res. Energy* 1 (2022) 9120015.
- [15] J. Tang, X. Li, Y. Ma, K. Wang, Z. Liu, Q. Zhang, Boosting exciton dissociation and charge transfer by regulating dielectric constant in polymer carbon nitride for CO_2 photoreduction, *Appl. Catal. B: Environ.* 327 (2023), 122417.
- [16] Z. Zhang, Y. Xu, Q. Zhang, S. Fang, H. Sun, W. Ou, C. Su, Semi-heterogeneous photo-Cu-dual-catalytic cross-coupling reactions using polymeric carbon nitrides, *Sci. Bull.* 67 (2022) 71–78.
- [17] Y. Dai, Y. Xiong, Control of selectivity in organic synthesis via heterogeneous photocatalysis under visible light, *Nano Research, Energy* 1 (2022) 9120006.
- [18] A. Meng, Z. Teng, Q. Zhang, C. Su, Intrinsic defects in polymeric carbon nitride for photocatalysis applications, *Chem. - Asian J.* 15 (2020) 3405–3415.
- [19] S. Bai, N. Zhang, C. Gao, Y. Xiong, Defect engineering in photocatalytic materials, *Nano Energy* 53 (2018) 296–336.
- [20] J. Tang, Q. Li, Y. Liu, N. Xu, K. Wang, Q. Zhang, W. Yang, Y. Fan, The interfacial charge transfer in triphenylphosphine-based COF/PCN heterojunctions and its promotional effects on photocatalytic hydrogen evolution, *Int. J. Hydrog. Energy* 46 (2021) 17666–17676.
- [21] H. Yang, B. Xu, S. Yuan, Q. Zhang, M. Zhang, T. Ohno, Synthesis of Y-doped CeO_2/PCN nanocomposited photocatalyst with promoted photoredox performance, *Appl. Catal. B: Environ.* 243 (2019) 513–521.

- [22] Y. Zhang, Q. Cao, X. Wu, Y. Xiao, A. Meng, Q. Zhang, Y. Yu, W.-D. Zhang, Efficient photocatalytic H₂ evolution and α -methylation of ketones from copper complex modified polymeric carbon nitride, *Chem. Eng. J.* 427 (2022), 132042.
- [23] J. Tang, X. Li, Y. Ma, N. Xu, Y. Liu, Q. Zhang, Formation of interfacial P-Ni-P coordination to boost charge transfer of polymeric carbon nitride for enhanced photocatalytic activity of H₂ evolution, *Appl. Surf. Sci.* 602 (2022), 154228.
- [24] H. Sun, K. Wei, D. Wu, Z. Jiang, H. Zhao, T. Wang, Q. Zhang, P.K. Wong, Structure defects promoted exciton dissociation and carrier separation for enhancing photocatalytic hydrogen evolution, *Appl. Catal. B: Environ.* 264 (2020), 118480.
- [25] Q. Liang, Z. Li, Z.-H. Huang, F. Kang, Q.-H. Yang, Holey graphitic carbon nitride nanosheets with carbon vacancies for highly improved photocatalytic hydrogen production, *Adv. Funct. Mater.* 25 (2015) 6885–6892.
- [26] P. Zhang, L.-J. Wu, W.-G. Pan, Z.-Z. Wei, X.-Y. Liang, R.-T. Guo, Granular polymeric carbon nitride with carbon vacancies for enhanced photocatalytic hydrogen evolution, *Sol. RRL* 5 (2021) 2000796.
- [27] F. Yang, H. Li, K. Pan, S. Wang, H. Sun, Y. Xie, Y. Xu, J. Wu, W. Zhou, Engineering surface N-vacancy defects of ultrathin mesoporous carbon nitride nanosheets as efficient visible-light-driven photocatalysts, *Sol. RRL* 5 (2020) 2000610.
- [28] Y. Xie, Y. Li, Z. Huang, J. Zhang, X. Jia, X.-S. Zhang, J. Ye, Two types of cooperative nitrogen vacancies in polymeric carbon nitride for efficient solar-driven H₂O₂ evolution, *Appl. Catal. B: Environ.* 265 (2020), 118581.
- [29] J. Xiao, J.W. Zhang, J. Zhang, L. Pan, C. Shi, X. Zhang, J.J. Zou, Synergy of iron doping and cyano groups for enhanced photocatalytic hydrogen production over g-C₃N₄, *Chem. – A Eur. J.* 27 (2021) 17628–17636.
- [30] H. Yu, R. Shi, Y. Zhao, T. Bian, Y. Zhao, C. Zhou, G.L.N. Waterhouse, L.Z. Wu, C. H. Tung, T. Zhang, Alkali-Assisted synthesis of nitrogen deficient graphitic carbon nitride with tunable band structures for efficient visible-light-driven hydrogen evolution, *Adv. Mater.* 29 (2017) 1605148.
- [31] D. Zhao, C.L. Dong, B. Wang, C. Chen, Y.C. Huang, Z. Diao, S. Li, L. Guo, S. Shen, Synergy of dopants and defects in graphitic carbon nitride with exceptionally modulated band structures for efficient photocatalytic oxygen evolution, *Adv. Mater.* 31 (2019) 1903545.
- [32] P. Xia, M. Antonietti, B. Zhu, T. Heil, J. Yu, S. Cao, Designing defective crystalline carbon nitride to enable selective CO₂ photoreduction in the gas phase, *Adv. Funct. Mater.* 29 (2019) 1900093.
- [33] P. Xia, B. Zhu, J. Yu, S. Cao, M. Jaroniec, Ultra-thin nanosheet assemblies of graphitic carbon nitride for enhanced photocatalytic CO₂ reduction, *J. Mater. Chem. A* 5 (2017) 3230–3238.
- [34] T. Zhang, W. Schilling, S.U. Khan, H.Y.V. Ching, C. Lu, J. Chen, A. Jaworski, G. Barcaro, S. Monti, K. De Wael, A. Slabon, S. Das, Atomic-Level understanding for the enhanced generation of hydrogen peroxide by the introduction of an aryl amino group in polymeric carbon nitrides, *ACS Catal.* 11 (2021) 14087–14101.
- [35] Y. Xu, M. Fan, W. Yang, Y. Xiao, L. Zeng, X. Wu, Q. Xu, C. Su, Q. He, Homogeneous carbon/potassium-incorporation strategy for synthesizing red polymeric carbon nitride capable of near-infrared photocatalytic H₂ production, *Adv. Mater.* 33 (2021) 2101455.
- [36] Q. Li, C. Ren, C. Qiu, T. He, Q. Zhang, X. Ling, Y. Xu, C. Su, Promoting near-infrared photocatalytic activity of carbon-doped carbon nitride via solid alkali activation, *Chin. Chem. Lett.* 32 (2021) 3463–3468.
- [37] Kuanhong Cao, Xin Deng, Tian Chen, Qitao Zhang, Lei Yu, A facile approach to constructing Pd@PCN-Se nano-composite catalysts for selective alcohol oxidation reactions, *J. Mater. Chem. A* 7 (2019) 10918.
- [38] H. Ou, P. Yang, L. Lin, M. Anpo, X. Wang, Carbon nitride aerogels for the photoredox conversion of water, *Angew. Chem. Int. Ed.* 56 (2017) 10905–10910.
- [39] Y. Xu, X. He, H. Zhong, D.J. Singh, L. Zhang, R. Wang, Solid salt confinement effect: an effective strategy to fabricate high crystalline polymer carbon nitride for enhanced photocatalytic hydrogen evolution, *Appl. Catal. B: Environ.* 246 (2019) 349–355.
- [40] C. Qiu, Y. Xu, X. Fan, D. Xu, R. Tandiana, X. Ling, Y. Jiang, C. Liu, L. Yu, W. Chen, C. Su, Highly crystalline k-intercalated polymeric carbon nitride for visible-light photocatalytic alkenes and alkynes deuteration, *Adv. Sci.* 6 (2019) 1801403.
- [41] K. Wang, J. Fu, Y. Zheng, Insights into photocatalytic CO₂ reduction on g-C₃N₄: Strategy of simultaneous B, K co-doping and enhancement by N vacancies, *Applied Catalysis B: Environmental* 254 (2019) 270–282.
- [42] W. Lin, H. Chen, G. Lin, S. Yao, Z. Zhang, J. Qi, M. Jing, W. Song, J. Li, X. Liu, J. Fu, S. Dai, Creating frustrated lewis pairs in defective boron carbon nitride for electrocatalytic nitrogen reduction to ammonia, *Angew. Chem. Int. Ed.* 61 (2022), 202207807.
- [43] Q. Liu, J. Lin, H. Cheng, L. Wei, F. Wang, Simultaneous co-Photocatalytic CO₂ reduction and ethanol oxidation towards synergistic acetaldehyde synthesis, *Angew. Chem. Int. Ed.* 62 (2023) 202218720.
- [44] X. Wu, R. Zhong, X. Lv, Z. Hu, D. Xia, C. Li, B. Song, S. Liu, Modulating g-C₃N₄-based van der Waals heterostructures with spatially separated reductive centers for tandem photocatalytic CO₂ methanation, *Appl. Catal. B: Environ.* 330 (2023), 122666.
- [45] M. Lu, M. Zhang, J. Liu, T.-Y. Yu, J.-N. Chang, L.-J. Shang, S.-L. Li, Y.-Q. Lan, Confining and highly dispersing single polyoxometalate clusters in covalent organic frameworks by covalent linkages for CO₂ photoreduction, *J. Am. Chem. Soc.* 144 (2022) 1861–1871.
- [46] Y.S. Xia, M. Tang, L. Zhang, J. Liu, C. Jiang, G.K. Gao, L.Z. Dong, L.G. Xie, Y.Q. Lan, Tandem utilization of CO₂ photoreduction products for the carbonylation of aryl iodides, *Nat. Commun.* 13 (2022) 2964.
- [47] M. Zhang, J.N. Chang, Y. Chen, M. Lu, T.Y. Yu, C. Jiang, S.L. Li, Y.P. Cai, Y.Q. Lan, Controllable Synthesis of COFs-Based multicomponent nanocomposites from core-shell to yolk-shell and hollow-sphere structure for artificial photosynthesis, *Adv. Mater.* 33 (2021) 2105002.
- [48] G. Zhang, Y. Xu, D. Yan, C. He, Y. Li, X. Ren, P. Zhang, H. Mi, Construction of K⁺ Ion gradient in crystalline carbon nitride to accelerate exciton dissociation and charge separation for visible light H₂ production, *ACS Catal.* 11 (2021) 6995–7005.
- [49] G. Zhang, Y. Xu, M. Rauf, J. Zhu, Y. Li, C. He, X. Ren, P. Zhang, H. Mi, Breaking the limitation of elevated coulomb interaction in crystalline carbon nitride for visible and near-infrared light photoactivity, *Adv. Sci.* 9 (2022) 2201677.
- [50] Z. Teng, W. Cai, S. Liu, C. Wang, Q. Zhang, S. Chenliang, T. Ohno, Bandgap engineering of polymetric carbon nitride copolymerized by 2,5,8-triamino-tri-s-triazine (melem) and barbituric acid for efficient nonsacrificial photocatalytic H₂O₂ production, *Appl. Catal. B: Environ.* 271 (2020), 118917.
- [51] J. Tang, Q. Zhang, Y. Liu, Y. Liu, K. Wang, N. Xu, L. Yu, Q. Tong, Y. Fan, The photocatalytic redox properties of polymeric carbon nitride nanocages (PCNCs) with mesoporous hollow spherical structures prepared by a ZnO-template method, *Microporous Mesoporous Mater.* 292 (2020), 109639.
- [52] M. Kou, Y. Wang, Y. Xu, L. Ye, Y. Huang, B. Jia, H. Li, J. Ren, Y. Deng, J. Chen, Y. Zhou, K. Lei, L. Wang, W. Liu, H. Huang, T. Ma, Molecularly engineered covalent organic frameworks for hydrogen peroxide photosynthesis, *Angew. Chem. Int. Ed.* 61 (2022), 202200413.
- [53] K. Kunimatsu, T. Yoda, D.A. Tryk, H. Uchida, M. Watanabe, In situ ATR-FTIR study of oxygen reduction at the Pt/Nafion interface, *Phys. Chem. Chem. Phys.* 12 (2010) 621–629.
- [54] S. Nayak, L.J. McPherson, K.A. Vincent, Adsorbed intermediates in oxygen reduction on platinum nanoparticles observed by in situ IR spectroscopy, *Angew. Chem. Int. Ed.* 57 (2018) 12855–12858.
- [55] M. Shao, P. Liu, R.R. Adzic, Superoxide anion is the intermediate in the oxygen reduction reaction on platinum electrodes, *J. Am. Chem. Soc.* 128 (2006) 7408–7409.
- [56] M. Chen, Y. Lin, Y. Lin, H. Lin, J. Lin, Dissociative adsorption of HCOOH, CH₃OH, and CH₂O on MCM-41, *J. Catal.* 228 (2004) 259–263.
- [57] C. Tang, L. Chen, H. Li, L. Li, Y. Jiao, Y. Zheng, H. Xu, K. Davey, S.Z. Qiao, Tailoring acidic oxygen reduction selectivity on single-atom catalysts via modification of first and second coordination spheres, *J. Am. Chem. Soc.* 143 (2021) 7819–7827.
- [58] D. Zhang, P. Ren, W. Liu, Y. Li, S. Salli, F. Han, W. Qiao, Y. Liu, Y. Fan, Y. Cui, Y. Shen, E. Richards, X. Wen, M.H. Rummeli, Y. Li, F. Besenbacher, H. Niemantsverdriet, T. Lim, R. Su, Photocatalytic abstraction of hydrogen atoms from water using hydroxylated graphitic carbon nitride for hydrogenative coupling reactions, *Angew. Chem. Int. Ed.* 61 (2022), 202204256.
- [59] R. Liang, S. Luo, F. Jing, L. Shen, N. Qin, L. Wu, A simple strategy for fabrication of Pd@MIL-100(Fe) nanocomposite as a visible-light-driven photocatalyst for the treatment of pharmaceuticals and personal care products (PPCPs), *Appl. Catal. B: Environ.* 176–177 (2015) 240–248.
- [60] J. Tang, T. Zhao, D. Solanki, X. Miao, W. Zhou, S. Hu, Selective hydrogen peroxide conversion tailored by surface, interface, and device engineering, *Joule* 5 (2021) 1432–1461.
- [61] J. Xu, X. Jiao, K. Zheng, W. Shao, S. Zhu, X. Li, J. Zhu, Y. Pan, Y. Sun, Y. Xie, Plastics-to-syngas photocatalysed by Co-Ga₂O₃ nanosheets, *Natl. Sci. Rev.* 9 (2022) nwac011.
- [62] R. Jiang, G. Lu, Z. Yan, D. Wu, R. Zhou, X. Bao, Insights into a CQD-SnNb₂O₆/BiOCl Z-scheme system for the degradation of benzocaine: influence factors, intermediate toxicity and photocatalytic mechanism, *Chem. Eng. J.* 374 (2019) 79–90.